

Effect of annealing atmosphere on LiMn<sub>2</sub>O<sub>4</sub> for thin film Li-ion batteries  
from aqueous chemical solution deposition

Peer-reviewed author version

MAINO, Giulia; D'HAEN, Jan; Mattelaer, F.; Detavernier, C.; HARDY, An & VAN  
BAEL, Marlies (2016) Effect of annealing atmosphere on LiMn<sub>2</sub>O<sub>4</sub> for thin film Li-ion  
batteries from aqueous chemical solution deposition. In: JOURNAL OF MATERIALS  
CHEMISTRY A, 4(47), p. 18457-18469.

DOI: 10.1039/c6ta08513j

Handle: <http://hdl.handle.net/1942/23272>

# Effect of annealing atmosphere on LiMn<sub>2</sub>O<sub>4</sub> for thin film Li-ion Batteries from aqueous Chemical Solution Deposition.

G. Maino,<sup>a</sup> J. D'Haen<sup>b</sup>, F. Mattelaer<sup>c</sup>, C. Detavernier<sup>c</sup>, A. Hardy<sup>a,d</sup> and M. K. Van Bael<sup>a,d</sup>

In this study we demonstrate and explain the direct relation between precursor chemistry and phase formation of LiMn<sub>2</sub>O<sub>4</sub> powders and thin films from aqueous chemical solution deposition (CSD). The processing conditions applied to transform the precursor into the LiMn<sub>2</sub>O<sub>4</sub> phase, are investigated with a focus on the heating atmosphere and temperature. We found that the Mn<sup>2+</sup> ions, used as a start product, already partially oxidizes into Mn<sup>3+</sup>/Mn<sup>4+</sup> in the precursor solution. The Mn<sup>3+</sup> ions present in the gel or the dried film are extremely sensitive to O<sub>2</sub>, leading to fast oxidation towards Mn<sup>4+</sup>. Here, we suggest that the oxygen, introduced in the precursor solution by the citrate complexing agent, suffices to oxidize the Mn<sup>2+</sup> into Mn<sup>3+</sup>/Mn<sup>4+</sup> which is crucial in the formation of phase pure spinel and stoichiometric LiMn<sub>2</sub>O<sub>4</sub>. Any additional oxygen, available as O<sub>2</sub> during the final processing, should be avoided as it leads to a further oxidation of the remaining Mn<sup>3+</sup> into Mn<sup>4+</sup> and to the formation of the γ-Mn<sub>2</sub>O<sub>3</sub> and λ-MnO<sub>2</sub> secondary phases. Based on these insights, the preparation of phase pure, spinel and stoichiometric LiMn<sub>2</sub>O<sub>4</sub> in a N<sub>2</sub> ambient was achieved both in powders and films. Moreover, the study of the precursor chemistry and final anneal leads to the possibility of reducing the final temperature to 450°C, enabling the use of temperature and oxidation sensitive current collectors such as TiN. This inert ambient and low temperature processing of LiMn<sub>2</sub>O<sub>4</sub> provides the opportunity to have large flexibility and compatibility with process conditions for other materials in the thin film battery stack, without undesired oxidations.

## Introduction

Portable / mobile electronics are indispensable in modern society. Continuous innovations increase their functionality, reduce size and weight, though at an increasing energy demand. Therefore, the development of improved, rechargeable batteries is simultaneously essential as well. The current generation of rechargeable batteries is dominated by powder based Li-ion technology, containing a cathode material, a separator that is soaked in electrolyte and an anode material. The electrolyte consists of a Li<sup>+</sup> salt dissolved in an organic liquid. The liquid electrolyte poses inherent risks, such as leakage and flammability. This leads to several restrictions in battery design and size. Thin film micro batteries emerged as valuable alternatives to these powder based batteries, and offer new opportunities: miniaturization and higher design flexibility. In addition, thin film micro batteries provide higher power and capacity and enhanced Li-ion conductivity<sup>1-4</sup>. Additionally, thin film micro batteries allow the use of solid electrolytes, yielding an all-solid-state Li-ion battery, removing the safety hazard, since no flammable solvents are present in this solid electrolyte. The thin film design prevents a large resistance over the electrolyte layer, as most solid electrolytes suffer from lower Li-ion conductivity compared to liquid electrolytes<sup>5,6</sup>.

All-solid-state Li-ion batteries eliminate the risk of leakage and open up other possibilities also in the medical field, e.g. power sources for safer and smaller medical implants.

LiMn<sub>2</sub>O<sub>4</sub> (LMO) emerges as the preferred cathode material for all-solid-state Li-ion batteries, because of its high energy density at high voltages (4 V region), as well as its high rate performance due to its 3D framework crystal structure<sup>7</sup>. A variety of cathode materials have been recently explored in literature, starting from LiCoO<sub>2</sub>, LiNiO<sub>2</sub>, reaching the

manganese based doped ones, so called "blended", such as LiNi<sub>0.8</sub>Co<sub>0.15</sub>Al<sub>0.05</sub>O<sub>2</sub> (NCA), LiNi<sub>1/3</sub>Mn<sub>1/3</sub>Co<sub>1/3</sub>O<sub>2</sub> (NMC). Among these cathode materials, LMO is thermally the most stable candidate. In fact, LMO exhibits the highest onset temperature (240°C) for exothermal processes, such as organic decomposition and releases a minimum amount of heat when charged up to 4.3V.<sup>8</sup> Additionally, LMO is advantageous due to its low cost, resource abundance, non-toxicity<sup>9</sup>, compared to the Co based materials. Although the blended cathodes exhibit a more balanced set of properties, due to obvious averaging of the materials characteristics, the effects of the blending are not straightforward. Complex interactions can be expected during the synthesis, deposition and during testing at relatively high operational rates. Un-doped LMO remains in fact, still a good alternative with comparable performances<sup>10</sup>. Various strategies are available for improving the cyclability and the thermostability of LMO-based batteries, confirming the wide interest in this material.<sup>11</sup> Currently, LMO films are prepared by high-cost, vacuum based methods such as sputtering, electron beam evaporation, pulsed-laser deposition and chemical vapor deposition<sup>12-19</sup>. Besides the high cost of these methods, they also suffer from limited stoichiometric control and long deposition times.

Chemical Solution Deposition (CSD)<sup>20,21</sup> routes are widely considered as an alternative to the vacuum based routes due to their low cost, simple experimental setup and high deposition rate<sup>22</sup>. Even epitaxial layers can be achieved via advantageous solutions routes using metalorganic precursors on different specific single crystals substrates<sup>23-25</sup>. Furthermore, CSD offers a good control over the homogeneity, stoichiometry, crystallinity, density and microstructure<sup>26</sup>. Nevertheless, in order to prepare LMO thin films via CSD, at least two requirements should be fulfilled: (i) intimate mixing of Mn<sup>2+</sup> and Li<sup>+</sup> should take place and (ii) phase segregation,

e.g. by formation and precipitation of polyanionic manganates or  $\text{Mn}(\text{OH})_2$ <sup>27</sup> should be prevented. To meet these requirements, both ions are stabilized using a citrate complex. After deposition, the precursor gel-film is converted into the desired, crystalline  $\text{LiMn}_2\text{O}_4$  through a series of thermal steps. During these thermal steps, (i) the network of citrate complexes, which is crucial to allow the deposition and to ensure an intimate mixing of the  $\text{Mn}^{2+}$  and  $\text{Li}^+$  ions, must be decomposed into volatile species, (ii) the oxide formation should take place and (iii) the crystallization of the desired spinel phase should occur. Because the decomposition and crystallization reactions take place during the calcination treatment, the annealing parameters (such as temperature, time and ambient) wherein these processes take place severely influence the quality of the obtained films.

Different studies have already highlighted the influence of annealing temperature on LMO thin films morphological and electrochemical properties. Park and co-workers<sup>28,29</sup> presented studies on synthesis of acetylacetonates based precursor in 1-butanol, in which they show the precursor decomposition starting from 230°C and continuing up to higher temperatures (i.e., above 400°C), where the rest of the organic materials can be easily and totally eliminated. After a drying step, the best conditions reported to obtain dense and relatively smooth film surface were 750°C for 10 mins in oxygen atmosphere. Ikuhara et al. conducted a study on precursor derived  $\text{LiMn}_2\text{O}_4$  thin films<sup>24</sup>, starting from isopropoxide and ethoxyethoxide precursors in 2-ethoxyethanol. They studied the crystallite size and orientation and show the possibility to obtain powders with heat treatment at low temperature and short period of time, without secondary phases (crystallization step up to 200-700°C for 3h in oxygen)<sup>30</sup>.

However, the use of oxygen atmosphere during post-anneal can lead to undesired oxidations both of the material itself, since Mn is very sensitive to oxidative conditions and its valence states are mutable, and the substrate chosen.

Previous groups that highlighted the atmosphere impact on the formation of phase pure and stoichiometric  $\text{LiMn}_2\text{O}_4$  powder based cathodes, synthesized by solid state reaction, are Nakamura's<sup>31</sup> and Strobel's<sup>32</sup>. Nakamura and co-workers<sup>31</sup> studied the effect of a low-temperature post-annealing (400°C for 20h) under various oxygen pressures of Li-Mn spinel oxide particles, that were oxygen deficient after a high temperature (850°C for 10h) solid state synthesis. It was found that the crystallinity and the performance of the material depend mainly on the oxygen stoichiometry. More specifically for the fixed Li/Mn molar ratio of 1:2, the lattice parameter of the cubic spinel decreased from 0.825 nm to 0.822 nm, with an increase in the oxygen pressure from 0 to 5 atm during annealing. This effect was ascribed to an increase in the average manganese valence (since the ionic radius of  $\text{Mn}^{4+}$  is smaller than that of  $\text{Mn}^{3+}$ ), which only occurs assuming the presence of oxygen vacancies in the as synthesized spinel phase. Moreover, the Li/Mn spinel oxide with a high average valence of Mn ions was found to have a minor variation in the oxidation state and a small stoichiometry change with

preparation conditions, while the one with a lower average valence of Mn ions close to 3.5, is very sensitive to the preparation conditions. Strobel et al.<sup>32</sup> also studied the effect of post-annealing conditions of Li/Mn spinel particles, prepared by a solid state reaction at high temperature. During annealing in oxidizing conditions, they observed the formation of trivalent manganese oxide  $\text{Mn}_2\text{O}_3$  secondary phases. The mechanism they propose, does not require the postulation of oxygen vacancies in the pristine material. Indeed, they found proof for a disproportionation of the stoichiometric  $\text{LiMn}_2\text{O}_4$  into a spinel with higher manganese valence that is compensated by the formation of the trivalent  $\text{Mn}_2\text{O}_3$ . In this context, the purpose of this paper is the in depth analysis of this material sensitivity and instability both on powders and films deposited via CSD, with emphasis on the atmosphere influence. The synthesis route proposed is fast and water based, excluding organic solvents, such as 2-methoxyethanol, 2-ethoxyethanol, 1-butanol or ethanol. Both metal precursors are nitrates based, which have the advantage to decompose at lower temperature, because of the presence of very oxidizing  $\text{NO}_3^-$  groups. Those groups are in fact active towards oxidative decomposition of citric acid. This results in relatively low calcination temperature (450°C) within a short time (1h), avoiding the formation of other manganese oxidation-state compounds as impurity, as would have been promoted by the use of acetate salts containing carbon<sup>33</sup>.

## Experimental

### Synthesis and characterization of the aqueous citrate- $\text{Mn}^{2+}$ , $\text{Li}^+$ precursor solution

The synthesis of the CSD precursor solution is schematized in Fig S1.

Manganese nitrate tetrahydrate ( $\text{Mn}(\text{NO}_3)_2 \cdot 4\text{H}_2\text{O}$ ,  $\geq 99\%$ , Sigma-Aldrich) is dissolved in water (0.2 M) while stirring. Next, citric acid ( $\text{C}_6\text{H}_8\text{O}_7$ ,  $\geq 99\%$ , Sigma-Aldrich) is added, in a citrate: $\text{Mn}^{2+}$  molar ratio of 3:1. In parallel, lithium nitrate ( $\text{LiNO}_3$ ,  $\geq 98\%$ , Sigma-Aldrich) is dissolved in water while stirring to obtain an aqueous  $\text{Li}^+$  solution (0.1 M). Both solutions are mixed with a  $\text{Mn}^{2+}$ :  $\text{Li}^+$  molar ratio 2:1. Ammonia ( $\text{NH}_3$ , 32% aqueous solution, Merck) is added to this mixture until a pH of 7 is reached (pH-Electrode, Sentix 60, 3 M KCl). Finally, the prepared solution is diluted with water to obtain an aqueous citrate- $\text{Mn}^{2+}$ ,  $\text{Li}^+$  precursor solution with Mn and Li concentrations of 0.2 M and 0.1 M, respectively. The concentrations are determined by means of inductively coupled plasma-atomic emission spectroscopy (ICP-AES, Perkin Elmer, Optima 3300 DV)<sup>34-39</sup>.

### Powder preparation and characterization

The precursor solution is dried overnight (air flow furnace, 60 °C) to obtain a gel powder for further analyses. Thermal decomposition of the dried precursor powder is examined by means of thermogravimetric (TGA) analysis, on-line coupled

with a differential scanning calorimetry (DSC) instrument. The thermogravimetric analyses are carried out in O<sub>2</sub> or N<sub>2</sub>, at a heating rate of 10°C min<sup>-1</sup> from room temperature to 600°C. The TG-DSC is performed on a Q600, TA Instrument (±3 mg of sample with a gas flow of 100 mL·min<sup>-1</sup>) coupled with a Pfeiffer Vacuum ThermoStar™ MS.

To form the oxide, the precursor powder is calcined in a tube furnace at 450 or 800 °C for 1 or 3 hours with a continuous O<sub>2</sub> or N<sub>2</sub> flow (100 mL·min<sup>-1</sup>), with a heating rate of 10°C min<sup>-1</sup> starting from room temperature. The precursor and thermally treated powders are characterized by (i) Fourier transform infra-red (FTIR) spectroscopy on a Bruker, Vertex 70 (32 scans, 4 cm<sup>-1</sup> resolution) dispersed in KBr pellets (1 wt %), (ii) Bruker AXS D8 diffractometer, equipped with a Göbel mirror (line focus, mostly Cu k<sub>α</sub> radiation). The diffractograms are recorded by a one-dimensional lynxeye detector. (iii) Raman spectroscopy on a Horiba Jobin Yvon micro-Raman (T64000) using a 488 nm laser (LEXEL 95 SHG) operating at 200 mW and (iv) Transmission electron microscopy (TEM) on FEI Microscope (Tecnai G2 Spirit Twin) operating at 120 kV, using the brightfield imaging mode. The samples for TEM are prepared by drying a few drops of a suspension of the synthesized powder in methanol on a holey carbon grid in ambient conditions under an IR lamp.

### Film preparation and characterization

For this study two types of substrates are used: (i) Si substrates with a native SiO<sub>2</sub> surface (±2.5cm\*2.5cm) and (ii) Pt substrates (80nm PVD Pt, on top of 40nm PVD TiN as lithium barrier and adhesion layer for the Pt)<sup>40</sup>. Before deposition, all substrates are treated in a UV-O<sub>3</sub> chamber at 80 °C (Novascan PSD Pro Series) for 40 min. The aqueous citrato-Mn<sup>2+</sup>, Li<sup>+</sup> precursor solution is deposited by spincoating (at a rotation speed of 3000 rpm, 30 s, with an acceleration of 1000 rpm·s<sup>-1</sup>). The as deposited layers are heated/calcined in a tube furnace at 450 or 800°C, with a heating rate of 10°C·min<sup>-1</sup>. The isothermal period is varied between 1 and 3 hours. As ambient gas oxygen (O<sub>2</sub>, 99,999%) or nitrogen (N<sub>2</sub>, 99,999%) are chosen, with a 100 ml·min<sup>-1</sup> flow. Due to the shape of the furnaces the setup is not fully airtight allowing, possibly, some minor traces of O<sub>2</sub>.

The prepared films, 100nm thick, are analyzed by Raman spectroscopy on a Horiba Jobin Yvon micro-Raman (T64000) using a 488 nm laser (LEXEL 95 SHG) operating at 200 mW. Grazing angle attenuated total reflectance-Fourier transform infrared (GATR-FTIR) spectroscopy is also performed on the films, using a 65° single reflection Ge-ATR (Harrick) crystal, placed inside the sample compartment of a FTIR spectrometer (Bruker, Vertex 70, 32 scans, 4 cm<sup>-1</sup> resolution). Crystallization behavior is studied by characterization of non-annealed samples by means of in-situ XRD (Bruker D8 Discover with experimental heating chamber)<sup>41,42</sup>, using 0.2 °C/s heating rate and O<sub>2</sub> or He flow. The films deposited on Pt/TiN/SiO<sub>2</sub>/Si substrate<sup>40</sup> are electrochemically tested as working electrodes in a galvanic cell, with lithium foils (Sigma, 1.5mm thick, 99% trace metal basis) as counter and reference electrodes. The

potentiostat used is Autolab PGSTAT128N. The electrolyte is a 1 M LiClO<sub>4</sub>/propylene carbon 1:2 solution. The cyclic voltammetry tests are carried out in Ar atmosphere in a Sylatech Environmental Chamber Glovebox. The film's morphology and thickness are visualized via scanning electron microscopy (SEM, FEI Quanta 200F), using the secondary electrons imaging mode, in a top-down and cross-sectional geometry, respectively.

## Results and Discussion

To determine the influence of the ambient wherein the oxide formation takes place, the thermal decomposition pathway of the precursor gel is compared. Furthermore the LiMn<sub>2</sub>O<sub>4</sub> oxide formation and crystallization, and the electrochemical performances after processing in an oxidative (O<sub>2</sub>) versus an inert (N<sub>2</sub>) atmosphere are examined.

### Thermal decomposition pathway of the citrato-Mn<sup>2+</sup>, Li<sup>+</sup> precursor gel

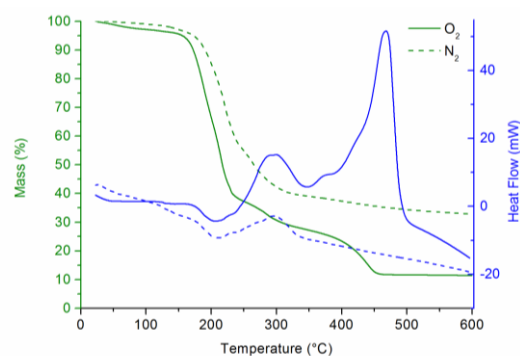


Figure 1: TGA (Mass%) and DSC (Heat flow) analysis of the dried citrate-Mn<sup>2+</sup>, Li<sup>+</sup> precursor gel. The analyses are performed in O<sub>2</sub> (solid line) and N<sub>2</sub> (dashed line).

The thermal decomposition pathway of the precursor gel is studied in O<sub>2</sub> and N<sub>2</sub> by TGA-DTG (Fig. S2) and TGA-DSC (Fig. 1). In both conditions, the weight loss occurs through a sequence of steps.

Up to 190°C the thermal decomposition pathway is very similar in O<sub>2</sub> and N<sub>2</sub>. In the first part, a small weight loss is observed around 100°C, which is ascribed to the evaporation of residual water from the precursor gel.

The first major decomposition steps occur between 175 °C and 250 °C during which mass fragments of NH<sub>3</sub><sup>+</sup>, OH<sup>+</sup>, H<sub>2</sub>O<sup>+</sup>, NH<sub>4</sub><sup>+</sup> and CO<sub>2</sub><sup>+</sup> were observed via mass spectrometry (Fig. S2). These fragments are assigned to the evolution of NH<sub>3</sub>, H<sub>2</sub>O and CO<sub>2</sub> and result from the decomposition of the excess of ammonium citrate into carboxylic acid groups and their subsequent decarboxylation, and the dehydroxylation of citrate's α-hydroxyl functionality<sup>43-45</sup>. Since these decompositions are endothermic, as indicated by the negative heat flow (with respect to its background level), and similarly occur in both atmospheres, they are non-oxidative decomposition reactions of the precursor<sup>7</sup>. Although the mass

fragments evolved are the same in both atmospheres, after 190°C the precursors underwent different chemical processes. The precursor analyzed in O<sub>2</sub> was subjected to a thermo-oxidative degradation, forming volatile radicals that evolve immediately after reacting with O<sub>2</sub>. Fragments related to NO<sup>+</sup>, C<sub>2</sub>H<sub>6</sub><sup>+</sup>, H<sub>2</sub>N=CH<sub>2</sub><sup>+</sup> (m/z 30), HNCO<sup>+</sup>, C<sub>2</sub>H<sub>7</sub><sup>+</sup> (m/z 43), CO<sub>2</sub><sup>+</sup>, H<sub>2</sub>N-C=O<sup>+</sup>, C<sub>3</sub>H<sub>8</sub><sup>+</sup> (m/z 44), evolve at lower temperatures (see Fig. S3(a-i)) in O<sub>2</sub>, and this might cause also the presence of a peak in the TGA-DTG (Fig. S2) at 190°C and the related mass loss. The precursor analyzed in N<sub>2</sub>, because of the inert atmosphere, is subjected only of thermal degradation, which can cause the formation of less volatile species and termination reactions of the radicals involved. Those intermediate compounds degrade at higher temperatures in N<sub>2</sub>, and this may cause the mass retention from 190°C up to 300°C. Their degradation partially continues around 300°C, where an exothermic peak can be noted in both atmospheres. From the TGA-DTG (Fig.S2) a difference can be seen in peak position and shape in this temperature region, and because of the different thermal processes involved in the two atmospheres, this is due to the different nature of the organic species left in the samples.

From 320°C onwards a clear difference is observed between the pathway in O<sub>2</sub> and N<sub>2</sub>. In O<sub>2</sub>, a major weight loss is seen between 430°C and 460°C with its decomposition rate maximum at 440 °C in the DSC curve (Fig.1). This weight loss is associated with a positive heat flow and does not occur in N<sub>2</sub>, suggesting that oxidative and exothermic processes occur in this temperature region. This decomposition step goes along with the LiMn<sub>2</sub>O<sub>4</sub> phase formation, as seen in Raman (Fig.5)<sup>46-48</sup> and results in a final mass of just above 10%, assigned to the LiMn<sub>2</sub>O<sub>4</sub> phase. Between 460 and 600 °C, no further weight loss or exothermic signal is observed in N<sub>2</sub>, leading to a final material with just above 30% residual mass (possibly about 10% final oxide and 20% of charred carbon left). Based on the TGA analyses 450°C was chosen as the calcination temperature for the powders and films.

### LiMn<sub>2</sub>O<sub>4</sub> oxide and spinel phase formation from the citrato-Mn<sup>2+</sup>, Li<sup>+</sup> precursor gel at 450°C

After calcining the precursor gels for 1h in N<sub>2</sub> and O<sub>2</sub> at 450°C, the powders are analyzed by means of Fourier Transform Infrared Spectroscopy.

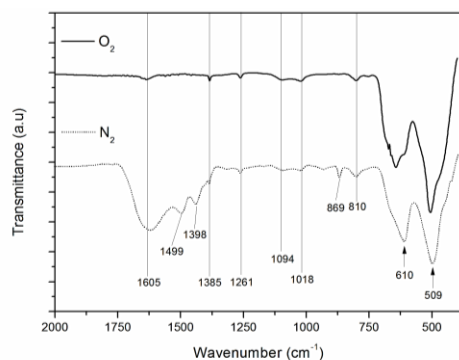


Table 1: Peak assignment of the powders obtained at 450°C for 1h in O<sub>2</sub> and N<sub>2</sub>.

Wavenumber	N <sub>2</sub> ambient	O <sub>2</sub> ambient	Vibrations Assignment
1583 cm <sup>-1</sup>	1605	1605	$\nu_{as}(\text{CO}_2^-)$ with $\text{NH}_4^+$
1500 cm <sup>-1</sup>	1499	x	$\nu_{as}(\text{CO}_3^{2-})$ in $\text{Li}_2\text{CO}_3$
1398 cm <sup>-1</sup>	1398	x	$\nu(\text{C}=\text{O})$ in $\text{COO}^-$ or $\text{CO}_3^{2-}$ in $\text{Li}_2\text{CO}_3$
1384 cm <sup>-1</sup>	1385	1385	$\delta(\text{NH}_4^+)$ in $\text{NH}_4^+$
1250 cm <sup>-1</sup>	1261	1261	$\nu(\text{C}-\text{N})$ in $-\text{CONHR}$
1100 cm <sup>-1</sup>	1094	1094	$\nu(\text{C}-\text{O})$ in $\text{C}-\text{OH}$
1000 cm <sup>-1</sup>	1018	1018	$\nu(\text{C}-\text{O})$ in $\text{C}-\text{OH}$
880 cm <sup>-1</sup>	869	x	$\nu_{out}$ of plane bend( $\text{CO}_3^{2-}$ ) in $\text{Li}_2\text{CO}_3$
815 cm <sup>-1</sup>	810	810	$\nu(\text{N}-\text{O})$ in $\text{RO}-\text{N}=\text{O}$
613 cm <sup>-1</sup>	610	613	$\nu(\text{O}-\text{Mn(IV)}-\text{O})$
514 cm <sup>-1</sup>	509	510	$\nu(\text{O}-\text{Mn(III)}-\text{O})$

The FTIR absorption between 613 and 514 cm<sup>-1</sup> is attributed to the stretching modes of the Mn-O bonds, present in either MnO<sub>6</sub> or MnO<sub>4</sub> groups, mostly assigned to MnO<sub>6</sub><sup>49-52</sup>, i.e., the stretching of O-Mn<sup>4+</sup>-O and Mn<sup>3+</sup>-O<sup>53</sup>, possibly of the spinel LiMn<sub>2</sub>O<sub>4</sub> phase. This indicates that the oxide is formed both in N<sub>2</sub> and O<sub>2</sub>, although the stretching at 514 cm<sup>-1</sup> is assigned to Mn<sup>3+</sup>-O (which is present in the desired LMO phase), while the stretching at 613 cm<sup>-1</sup> is assigned to Mn<sup>4+</sup>-O (which can be due to the presence of undesired Mn<sup>4+</sup> secondary phases) as confirmed by XRD (Fig.3) further on. Because of the missing combustion step at 450°C, the powder annealed in N<sub>2</sub> contains more organic residues, as expected from the TGA-DSC curve (Fig.1). The FTIR results for N<sub>2</sub> anneal indeed show vibrations of groups from the precursor complex (C-O in C-OH, amides and nitrates) (Table.1) and the presence of carbonates (CO<sub>3</sub><sup>2-</sup>), due to the possible presence of lithium carbonate from the aging of the powders in air<sup>54,55</sup>. This compound is previously reported in other Li metal oxides, such as LiCoO<sub>2</sub><sup>56,57</sup>. Similar powders were analyzed via XRD to study the different oxide formation at 450 °C in O<sub>2</sub> versus N<sub>2</sub>.

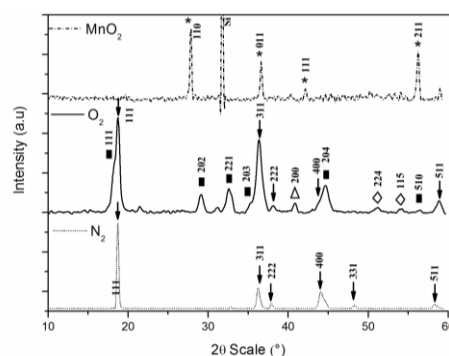


Figure 3: XRD of powders obtained at 450°C for 1h in N<sub>2</sub> and O<sub>2</sub> versus XRD of commercial MnO<sub>2</sub> powder. Arrow represents LiMn<sub>2</sub>O<sub>4</sub> face centered cubic spinel phase (JCPDS 89-0117), square represents gamma Mn<sub>2</sub>O<sub>3</sub> tetragonal (JCPDS 06-0540), star represent commercial MnO<sub>2</sub> powder (confirmed by JCPDS 50-0866) triangle represents MnO

face centered cubic (JCPDS 75-0626), diamond represents  $\text{Li}_2\text{MnO}_3$  base centered monoclinic (JCPDS 84-1634)

The XRD pattern in Fig.3 shows the main peaks of the LMO phase (peaks indexed with (111), (311), (222), (400), (331), (511) are clearly visible) for powder annealed in  $\text{N}_2$ . In samples annealed in  $\text{O}_2$ , similar diffractions peaks are present for the LMO phase, but also possible phase segregation is shown. Indeed, peaks indexed with (111), (202), (221), (203), (204), (510) suggest the formation of  $\gamma\text{-Mn}_2\text{O}_3$  in tetragonal phase. This phase may have been formed by disproportionation of the initial  $\text{Mn}^{3.5+}$  (average oxidation state) present in LMO into  $\text{Mn}^{3+}$  and  $\text{Mn}^{3.5+\delta}$ , following the mechanism posed by Strobel<sup>32</sup>, with the difference that here the disproportionation occurs already during the formation of the spinel phase, and not after. A small fraction of  $\text{MnO}$  and  $\text{Li}_2\text{MnO}_3$  is also observed, possibly due to the instability of the cubic spinel. No secondary  $\text{MnO}_2$  phase is observed, as confirmed by the comparison with  $\text{MnO}_2$  commercial powder. Raman spectra are recorded to give further insights based on the vibration modes of  $\text{Mn}^{3+}/\text{Mn}^{4+}\text{-O}$  chemical bonds after heat treatment at  $450^\circ\text{C}$ . These features could allow detecting the presence of  $\text{Mn}^{4+}$  species (such as  $\text{MnO}_2$ ) which are not necessarily seen in the XRD patterns, for instance in case they are amorphous.

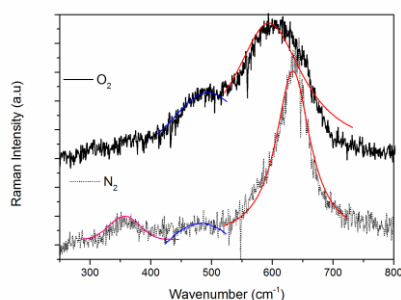


Figure 4: Raman spectra of powders obtained at  $450^\circ\text{C}$  for 1h in  $\text{N}_2$  and  $\text{O}_2$

Table 2: Deconvolution and Peak assignment<sup>58,59</sup> of the Raman spectra of powders obtained at  $450^\circ\text{C}$  for 1h in  $\text{N}_2$  and  $\text{O}_2$ .

Legend	Wavenumber ( $\text{cm}^{-1}$ ) in $\text{N}_2$ ambient	Wavenumber ( $\text{cm}^{-1}$ ) in $\text{O}_2$ ambient	Species Involved	Vibrational Modes
Red	643	600	$A_{1g}$	Mn-O in $\text{MnO}_6$
Blue	478	497	$F_{2g}(2)$	Mn-O in $\text{MnO}_6$
Magenta	382	x	$F_{2g}(3)$	Li-O connected to the tetrahedral cation movements

The  $\text{LiMn}_2\text{O}_4$  spinel exhibits a cubic structure, with space group  $Fd\bar{3}m$  ( $O_h^7$ ). In this structure, the anions occupy  $C_{3v}$  sites (32e Wyckoff position), Li atoms are located on tetrahedral sites of  $T_d$  symmetry and Mn atoms on octahedral sites of  $D_{3d}$  symmetry<sup>60</sup>.

A common feature in the Raman spectra of the two samples is the presence of a strong band around  $600\text{ cm}^{-1}$  and a group of bands between  $200$  and  $500\text{ cm}^{-1}$  with weaker intensity.

In spinel LMO and in other manganese oxides, wavenumbers of  $500\text{--}600\text{ cm}^{-1}$  are often assigned as characteristic of vibrations involving motion of oxygen atoms inside the

octahedral  $\text{MnO}_6$  unit<sup>61</sup>. So, peaks observed here between  $613$  and  $514\text{ cm}^{-1}$  (red and blue in Fig.4 and Table.2) were attributed to the stretching modes of the  $\text{MnO}_6$  based on these previous studies taken from literature<sup>51,52,61,62</sup>.

The spectra of the samples annealed in  $\text{N}_2$  and  $\text{O}_2$  show two large differences: peak broadness and peak position. The first can have different explanations: i) grain size, ii) presence of secondary phases, iii) amorphous phases<sup>61</sup>. i) The broadening is not due to the size of the crystallites, which is similar in both cases as demonstrated by TEM micrographs of the same thermally treated precursor gels, shown in (Fig.S4).

The precursor gel calcined at  $450^\circ\text{C}$  in  $\text{O}_2$  results in crystalline particles, generally adopted for spinel  $\text{LiMn}_2\text{O}_4$ <sup>63-65</sup>. The powder obtained at  $450^\circ\text{C}$  in  $\text{N}_2$  shows also similar shaped particles, immersed in an amorphous organic matrix. The organic nature of that matrix is previously studied by FTIR (Fig.2). Nevertheless this powder shows crystallites after a heat treatment in inert atmosphere, suggesting that no additional oxygen is required to oxidize and crystallize the spinel phase (see also Fig.3) from this precursor system (containing the specific precursor chemistry, solvents and chelating agents). The size of the crystallites after treatment in either  $\text{O}_2$  or  $\text{N}_2$  is quite similar ( $150\text{ nm} - 200\text{ nm}$ ), which confirms that the broadness of the Raman peaks is not due to different crystallite sizes. ii) From the XRD in Fig.3 different secondary phases are present in sample annealed in  $\text{O}_2$ .  $\gamma\text{-Mn}_2\text{O}_3$ <sup>66</sup>,  $\text{Li}_2\text{MnO}_3$ <sup>67</sup>,  $\text{MnO}$ <sup>68</sup> also show Mn-O vibrations in a similar range (around  $600\text{ cm}^{-1}$ ), which can indeed have an effect on the broadening of the peak. iii) Raman yields a complete and reliable description of materials such as the manganese oxides, because it is also sensitive towards amorphous components and materials where crystalline disorder may be expected<sup>61</sup>.

The shoulder appears also to shift towards lower wavelength. Regarding this shift, several studies suggest<sup>58,59</sup> that the intensity of the Raman shoulder at  $600\text{ cm}^{-1}$  is closely related to the manganese average oxidation state in the spinel phase. Because the intensity of this shoulder is very sensitive to the lithium stoichiometry and therefore manganese oxidation state, it might originate mainly from the  $\text{Mn}^{4+}\text{-O}$  vibration<sup>69</sup>.

As studied by Julien et al.<sup>70</sup>, the comparison of the Raman spectra of  $\text{LiMn}_2\text{O}_4$  and different  $\text{Mn}^{4+}$  compounds shows a shift towards different wavenumbers when  $\text{Li}^+$  is added to the crystal structure. More specifically, in case of  $\lambda\text{-MnO}_2$ , the wavenumber of the  $F_{2g}$  modes is expected to increase, while the wavenumber of the  $A_{1g}$  mode is predicted to decrease.

As can be seen in Table 2, the peak of the  $F_{2g}$  modes located at  $478\text{ cm}^{-1}$  in the sample heated in  $\text{N}_2$ , shifts towards higher wavenumber ( $497\text{ cm}^{-1}$ ) in sample treated in  $\text{O}_2$ , and the peak of the  $A_{1g}$  located at  $643\text{ cm}^{-1}$  in sample treated in  $\text{N}_2$ , shifts towards lower wavenumber ( $600\text{ cm}^{-1}$ ) in sample calcined in  $\text{O}_2$ , as expected from Julien et al. experimental finding<sup>70</sup>. It can be assumed that the treatment in  $\text{O}_2$  leads to the oxidation of the Mn-ions with an average oxidation state of  $+3.5$  (required for LMO) to  $+4$ , as would be corroborated by the presence of tetravalent manganese oxides, e.g.  $\lambda\text{-MnO}_2$ .

These  $\text{Mn-O}^{\text{IV}}$  phases were not detected by XRD (Fig.3), which still does not exclude their presence, if they are amorphous.

For the same reason, all the peaks in the Raman spectra of the powders treated in O<sub>2</sub> present a shift compared to the spectrum of pristine λ-MnO<sub>2</sub>. The F<sub>2g</sub> (3) mode at 382 cm<sup>-1</sup> due to the Li-O vibration is absent in the Raman spectrum of the powder treated in O<sub>2</sub>, like for the fully delithiated λ-MnO<sub>2</sub> phase.

So far, the crystallization of LMO powder at relatively low temperature (450°C) in inert atmosphere is shown. This leads to the hypothesis that no external O<sub>2</sub> needs to be provided during the calcination. In this conditions, powders show phase segregation in the XRD (Fig.3), broadening in the Raman peak (Fig.4) due to several factors already explained and a shift in the latter which can be possibly assigned to the presence of Mn<sup>4+</sup> species (such as λ-MnO<sub>2</sub>), not yet crystalline due to the low annealing temperature.

### Preparation of crystalline, spinel LiMn<sub>2</sub>O<sub>4</sub> films on non-conductive (SiO<sub>2</sub>) substrates at 450°C

The insights obtained with the formation of powder LMO from the aqueous precursor system, are used to aid in the understanding of the phase formation of LiMn<sub>2</sub>O<sub>4</sub> as a thin film cathode for an all solid-state Li-ion battery. For this purpose, the precursor solution is spin coated on two different substrates: SiO<sub>2</sub>/Si and platinized Si. The SiO<sub>2</sub> was chosen due to cost, thermal stability and chemical inertness towards manganese oxides<sup>71</sup> and the study of the phase formation on SiO<sub>2</sub> is intended to understand the difference between a thermal treatment in O<sub>2</sub> and N<sub>2</sub>, in the oxide formation, crystallization and morphology of the obtained films. The optimized processing is subsequently transferred to Pt, with similar films features in the studied conditions (Fig.S5,S6,S7,S8), for the evaluation of the electrochemical activity of the obtained spinel LiMn<sub>2</sub>O<sub>4</sub> film. The Pt substrates have a 40 nm thick TiN buffer layer to prevent lithium diffusion into the Si<sup>72</sup>.

In-situ XRD on spincoated films is carried out, to analyze in situ their crystallization behavior in both O<sub>2</sub> and N<sub>2</sub> atmospheres (Fig.S9). Other LMO in-situ XRD studies were already done for different purposes<sup>73-75</sup>. The onset of crystallization into the spinel LiMn<sub>2</sub>O<sub>4</sub> is observed at 360 °C and 400 °C in O<sub>2</sub> and N<sub>2</sub>, respectively, by the appearance of its (111) reflection at a 2θ value of 18,8°. This result is comparable with the XRD on powders shown in Fig.3. As the temperature increases, the amount of crystalline material increases as well, as is observed by the increase in the intensity of the diffraction peaks. The amount of crystalline material can suggest more pronounced crystallization in inert atmosphere.

Residual organic and inorganic compounds present in the films are analyzed by GATR-FTIR spectroscopy (Fig.5).

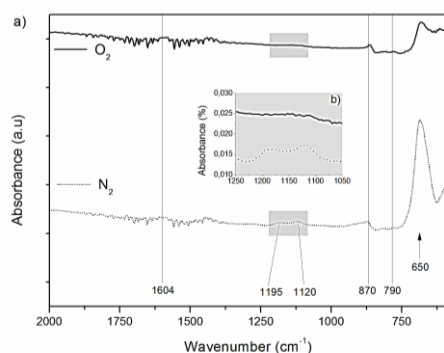


Figure 5: a) GATR-FTIR spectra of spincoated films on Si substrate, treated at 450°C for 1h in O<sub>2</sub> and N<sub>2</sub>, b) inset enlargement of the central region

Table 3: Peak assignment of films annealed at 450°C for 1h in O<sub>2</sub> and

Wavenumber	N <sub>2</sub>		Vibrations Assignment
	ambient	O <sub>2</sub> ambient	
1750-1450 cm <sup>-1</sup>	1604	1604	Rotational fine structure of gaseous H <sub>2</sub> O
1250 cm <sup>-1</sup>	1195	X	v(C-N) in -CONHR
1100 cm <sup>-1</sup>	1120	X	v(C-O) in C-OH
880 cm <sup>-1</sup>	870	870	v <sub>out of plane bend</sub> (CO <sub>3</sub> <sup>2-</sup> )
810 cm <sup>-1</sup>	790	790	v(N-O) in RO-N=O
622 cm <sup>-1</sup>	650	650	v(O-Mn-O)

Films calcined in both N<sub>2</sub> and O<sub>2</sub> show few organic residues (mostly due to citric acid decomposition and presence of water)<sup>76</sup>, but carbonates (CO<sub>3</sub><sup>2-</sup>) are also observed, due to lithium carbonate presence. The latter is possibly due to the same aging process assumed for powders (Fig.2)<sup>54,55</sup>.

By comparing both spectra (Fig.5b), it can be observed that more organics are removed during the processing in O<sub>2</sub>, while in films heated in N<sub>2</sub>, stretching absorptions of -CONHR (1250 cm<sup>-1</sup>) and -COH (1100 cm<sup>-1</sup>) are still present. The spectrum of the film treated in N<sub>2</sub> is dominated by strong absorption bands at 650 cm<sup>-1</sup>, assigned to the stretching mode of Mn-O in the MnO<sub>6</sub> group. This confirms the presence of metal-oxygen (Mn-O) bond<sup>77</sup>. For samples annealed in N<sub>2</sub>, the metal oxygen bond is more pronounced, indicating a clear presence of an oxide. This matches with XRD results (Fig.6), which confirm the presence of LMO.

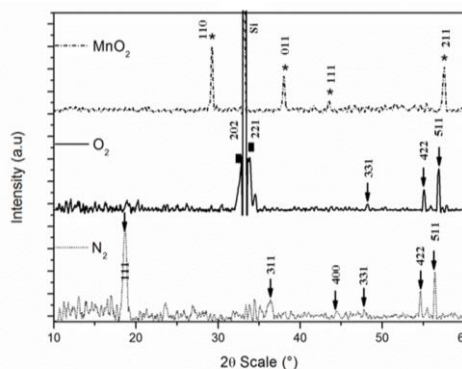


Figure 6: XRD of films on Si substrates, annealed at 450°C for 1h in N<sub>2</sub> and O<sub>2</sub> versus XRD of commercial MnO<sub>2</sub> powder. Arrow represents LiMn<sub>2</sub>O<sub>4</sub> face centered cubic spinel phase (JCPDS 89-0117), square represents gamma Mn<sub>2</sub>O<sub>3</sub> tetragonal (JCPDS 06-0540), star represent commercial MnO<sub>2</sub> powder (confirmed by JCPDS 50-0866)

The diffraction pattern shows that in films calcined in O<sub>2</sub> the main peak of LMO (111) is not present, although other peaks (such as (331), (422), (511) are found. This suggests that the LMO phase is present but has a different (preferential) orientation, as can be expected from the different morphology observed in the SEM study (Fig.8). A common peak at 33° is due to the Si substrate. The pattern shows that  $\gamma$ -Mn<sub>2</sub>O<sub>3</sub> is present in the film, as was observed in powders calcined under the same conditions (Fig.4). Note that no crystalline MnO<sub>2</sub> is detected in films annealed at 450°C in O<sub>2</sub>.

Raman spectra (Fig.7) are recorded to conduct the same study provided on powders (Fig.4).

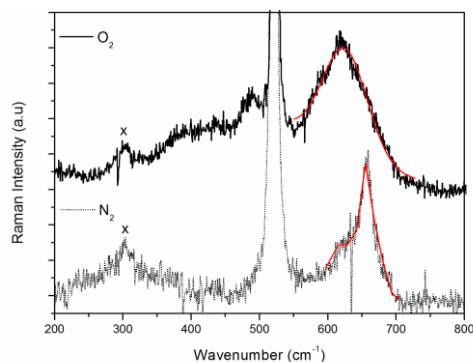


Figure 7: Raman spectra of films on Si/SiO<sub>2</sub> substrates treated at 450°C for 1h in N<sub>2</sub> and O<sub>2</sub>. In red the deconvoluted peak contours are drawn

Table 4: Deconvolution and Peak assignment<sup>58,59</sup> of films on Si substrates annealed at 450°C for 1h in N<sub>2</sub> and O<sub>2</sub>

Legend	Wavenumber (cm <sup>-1</sup> )	Wavenumber (cm <sup>-1</sup> )	Species	Vibrational Modes
	in N <sub>2</sub> ambient	in O <sub>2</sub> ambient		
Red	656	617	A <sub>1g</sub>	Mn-O in MnO <sub>6</sub> Li-O connected to
x	310	310	F <sub>2g</sub> (3)	the tetrahedral cation movements

Similar to the powders (Fig.4), also for the films exhibit a large difference in peak broadness and position for the shoulder around 600 cm<sup>-1</sup>. The peak broadness can also in the case of films be motivated by the presence of  $\gamma$ -Mn<sub>2</sub>O<sub>3</sub> and/or amorphous oxide phases<sup>61</sup>, not detected via XRD. The peak position can be related to the manganese average oxidation state in the spinel phase. It can be seen from the comparison that the A<sub>1g</sub> mode is shifting towards lower wavenumber in the film treated in O<sub>2</sub> (617 cm<sup>-1</sup> compared to 656 cm<sup>-1</sup> for the sample treated in N<sub>2</sub>), as expected from the study of Julien et al.<sup>70</sup> for  $\lambda$ -MnO<sub>2</sub>. A weaker peak is detected for both conditions around 310 cm<sup>-1</sup>, assigned to Li-O vibrations, connected to the tetrahedral cation movements. Both films show the presence of Li-O vibrations, indicative of the presence of LMO phase in both conditions, as was confirmed by XRD (Fig.6). It can be assumed that, also for films, treatment in O<sub>2</sub> may lead to phase segregation and possible formation of amorphous  $\lambda$ -MnO<sub>2</sub> as a consequence of oxidation of the Mn ions in LiMn<sub>2</sub>O<sub>4</sub> from an average oxidation state of +3.5 to +4. As was the case

for powders, also in the films no  $\lambda$ -MnO<sub>2</sub> crystalline phase could be detected in XRD (Fig.6) after a heat treatment at 450°C. Also here, this still could mean that an amorphous tetravalent manganese oxide has formed.

The morphology of the films, being very important for applications, is investigated (Fig.8), after heat treatment in O<sub>2</sub> and N<sub>2</sub> (450 °C) using SEM.

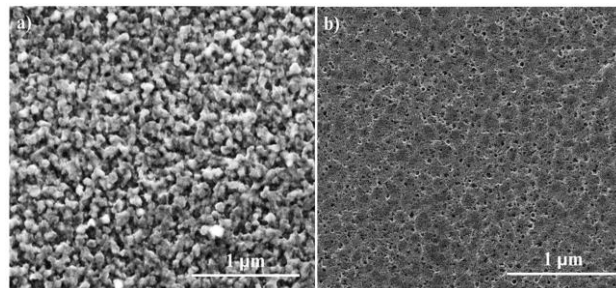


Figure 8: SEM Pictures of films on Si substrates, annealed in a) N<sub>2</sub> and b) O<sub>2</sub> at 450°C for 1h at 10°C/min.

The film heat treated in N<sub>2</sub> shows a more pronounced and better defined grain growth, in comparison to the film annealed in O<sub>2</sub>. However, both films are porous, and the porosity is distributed more evenly in the N<sub>2</sub> film. The presence of clear crystallites in this film can also suggest a higher crystallinity of the layer, compared to the film annealed in O<sub>2</sub>. It looks also more polycrystalline, and this can also explain the presence of more peaks in the XRD diffractogram (Fig.6).

#### LiMn<sub>2</sub>O<sub>4</sub> oxide and spinel phase formation from the citrato-Mn<sup>2+</sup>,Li<sup>+</sup> precursor gel at 800°C

The gels were also subjected to a heat treatment at 800°C for 3h. This treatment is chosen to allow tetravalent manganese phases to crystallize<sup>39,78</sup> and confirm the possible presence of Mn<sup>4+</sup> species, such as  $\lambda$ -MnO<sub>2</sub> which are still amorphous at 450°C.

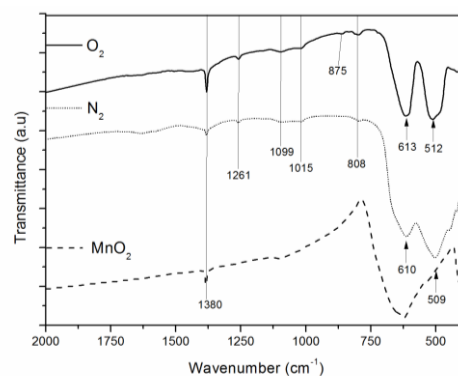


Figure 9: FTIR spectrum of powders obtained at 800°C for 3h in O<sub>2</sub> and N<sub>2</sub>

Table 5: Peak assignment of powders obtained at 800°C for 3h in O<sub>2</sub> and N<sub>2</sub>

Wavenumber	N <sub>2</sub> ambient	O <sub>2</sub> ambient	$\lambda$ -MnO <sub>2</sub>	Vibrations Assignment
1384 cm <sup>-1</sup>	1380	1380	1380	$\delta(\text{NH}_4^+)$ in NH <sub>4</sub> <sup>+</sup>
1250 cm <sup>-1</sup>	1261	1261	x	$\nu(\text{C-N})$ in -CONHR
1100 cm <sup>-1</sup>	1099	1099	x	$\nu(\text{C-O})$ in C-OH
1000 cm <sup>-1</sup>	1015	1015	x	$\nu(\text{C-O})$ in C-OH
880 cm <sup>-1</sup>	x	875	x	$\nu_{\text{out of plane bend}}(\text{CO}_3^{2-})$ in Li <sub>2</sub> CO <sub>3</sub>

IR spectra in Fig.9 show that the total amount of organic residues is lower than the one of the powders treated at 450°C, due to the higher thermal budget (longer time and higher temperature). Still, more organic residues from the precursor complex (C-OH, amides and nitrates in Table 5) are present in the sample annealed in inert atmosphere, although those signals are less pronounced than in Fig.2. The powder treated in N<sub>2</sub> shows an intense 509 cm<sup>-1</sup> vibrational mode of Mn(III)-O (3:1 peak area compared to the mode at 610 cm<sup>-1</sup>), while for powder annealed in O<sub>2</sub> there is an equivalent stretching with Mn(IV) ions (1:1 peak area compared to the one at 512 cm<sup>-1</sup>) at 613 cm<sup>-1</sup>.

XRD analysis on the same powders is shown (Fig.10).

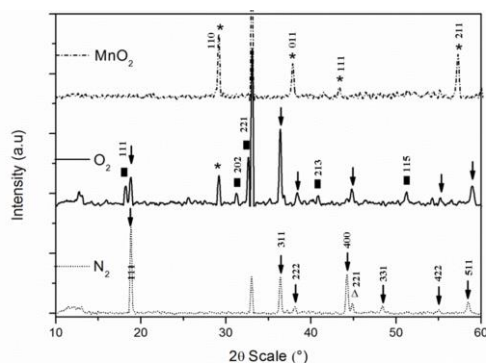


Figure 10: XRD of powders obtained at 800°C for 3h in N<sub>2</sub> and O<sub>2</sub> versus XRD of commercial MnO<sub>2</sub> powder. Arrow represents LiMn<sub>2</sub>O<sub>4</sub> face centered cubic spinel phase (JCPDS 89-0117), square represents gamma Mn<sub>2</sub>O<sub>3</sub> tetragonal (JCPDS 06-0540), triangle represents Li<sub>2</sub>MnO<sub>3</sub> based centered monoclinic JCPDS 84-1634), star represent commercial MnO<sub>2</sub> powder (confirmed by JCPDS 50-0866)

A thermal treatment in N<sub>2</sub> yields a material showing the main peaks of the LMO phase. Minor amounts of Li<sub>2</sub>MnO<sub>3</sub> are found, as was previously observed in the powders treated at 450°C as well (Fig.4). Samples annealed in O<sub>2</sub> contain the LMO phase (diffractions of (111), (311), (222), (400), (422), (511)) together with secondary phases. The tetragonal γ-Mn<sub>2</sub>O<sub>3</sub> phase is strongly present, besides a MnO<sub>2</sub> phase<sup>79</sup>, which was absent in samples annealed at 450°C. These observations may suggest that the disproportionation mechanism<sup>32</sup> is occurring and is influenced by the atmosphere, but also the temperature and the time of the annealing. During the heat treatment at higher

temperatures in O<sub>2</sub>, more Mn<sup>4+</sup> secondary phase crystallizes, as obvious already from the FTIR spectrum (Fig.9).

Raman spectra (Fig.11) are shown to study and possibly confirm the same phenomenon shown on powders (Fig.4), in samples annealed at higher temperatures.

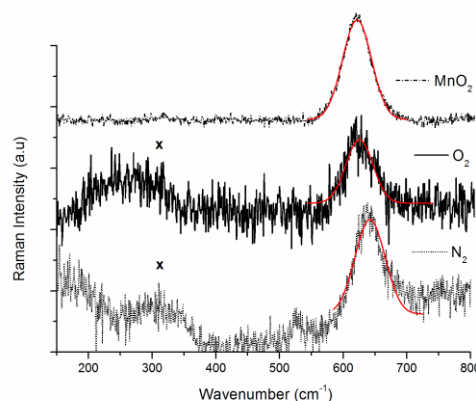


Figure 11: Raman spectra of powders obtained at 800°C for 3h in N<sub>2</sub> and O<sub>2</sub>.

Table 6: Deconvolution and Peak assignment<sup>58,59</sup> of the Raman spectra of powders obtained at 800°C for 3h in N<sub>2</sub> and O<sub>2</sub>.

Legend	Wavenumber (cm <sup>-1</sup> ) in N <sub>2</sub> ambient	Wavenumber (cm <sup>-1</sup> ) in O <sub>2</sub> ambient	Wavenumber (cm <sup>-1</sup> ) in MnO <sub>2</sub>	Species Involved	Vibrational Mode:
Red	650	620	620	A <sub>1g</sub>	Mn-O in MnO <sub>6</sub> Li-O connected to
x	310	310	x	F <sub>2g</sub> (3)	the tetrahedral cation movement:

Comparison of the Raman spectra of the powders, heated at 800°C in N<sub>2</sub> and O<sub>2</sub>, indicates that the A<sub>1g</sub> peak, located at 650 cm<sup>-1</sup> in the N<sub>2</sub> treated powder, shifts towards lower wavenumber (Table 6). This shift is in accordance with the model proposed by Julien et al.<sup>70</sup>. The similarity of the spectrum of the powder treated in O<sub>2</sub> with the MnO<sub>2</sub> spectrum, leads to the assumption that the O<sub>2</sub> gas oxidizes the Mn-ions present in the precursor to +4, leading to tetravalent Mn secondary phases already detected in XRD (Fig.10).

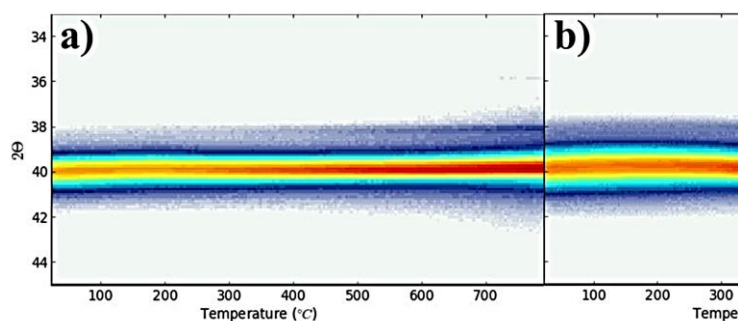


Figure 12: In-situ HT XRD of a film between  $2\theta$  values of  $33^\circ$  and  $45^\circ$ , obtained by spin coating of the precursor solution on Pt/TiN/SiO<sub>2</sub>/Si, recorded in a) N<sub>2</sub> and b) O<sub>2</sub> at a heating rate of 12 °C.min<sup>-1</sup>. The peak at  $40^\circ(2\theta)$  is assigned to the (111) reflection of the Pt substrate.

### Preparation of crystalline, spinel LiMn<sub>2</sub>O<sub>4</sub> films on non-conductive (SiO<sub>2</sub>) and conductive (Pt) substrates at 800°C

To follow in situ the crystallization of possible Mn<sup>4+</sup> species, especially MnO<sub>2</sub> known to crystallize around 800°C, in situ XRD on films is performed. The analysis was done from room temperature to 800°C, at a heating rate of 12°C/min, followed by an isothermal period of 1h at 800°C (Fig. 12). The analysis was performed on films deposited on a Pt substrate, in order to allow comparison with the films used for electrochemical characterization. Already at 400°C, the onset of MnO<sub>2</sub> phase formation is observed by the appearance of the (011) reflection at  $36^\circ(2\theta)$  in O<sub>2</sub> (Fig.12b). As the temperature rises, the amount of crystalline material further increases as seen by the increase of the intensity of the (011) reflection. This peak is not observed in inert conditions (Fig.12a). Thus, if the same sample is treated in O<sub>2</sub>, the LMO (crystalline at 450°C from Fig.S9 and Fig.6 and by the appearance of the (222) peak in both conditions from Fig.12a,b) partially oxidizes to MnO<sub>2</sub>. An 'off-line' XRD measurement (Fig.13) was carried out after cooling to room temperature of a film on Si/SiO<sub>2</sub> subjected to similar temperature profile (10°C/min instead of 12°C/min), for comparison.

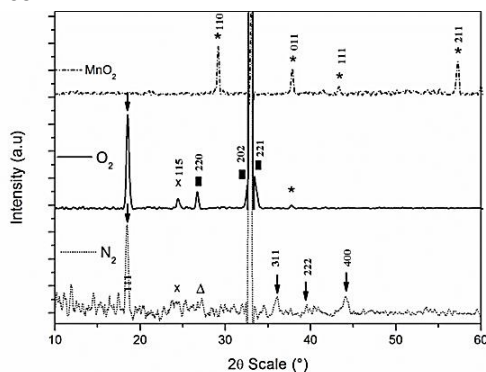


Figure 13: XRD of films on Si substrates, heated at 800°C for 3h in N<sub>2</sub> and O<sub>2</sub>. Arrow represents LiMn<sub>2</sub>O<sub>4</sub> face centered cubic spinel phase (JCPDS 89-0117), square represents gamma Mn<sub>2</sub>O<sub>3</sub> tetragonal (JCPDS 06-0540), star represent commercial MnO<sub>2</sub> powder (confirmed by JCPDS 50-0866), triangle represents Li<sub>2</sub>MnO<sub>3</sub> base centered monoclinic (JCPDS 84-1634), x represent Al<sub>2</sub>O<sub>3</sub> body centered tetragonal (JCPDS 16-0394)

The patterns show films with no preferential orientation. It must be noted that a small fraction of Al<sub>2</sub>O<sub>3</sub> is present (24%),

possibly due to the sample holder. After the high temperature treatment in N<sub>2</sub> the crystalline cubic LMO spinel phase is present (Fig.13) (diffractions (111), (311), (222), (400)), as was the case for powders (Fig.10). Although O<sub>2</sub> as ambient gas also yields the LMO phase, also secondary phases are observed in contrast to the anneal in N<sub>2</sub>. The secondary phase (Li<sub>2</sub>MnO<sub>3</sub>) was already observed on powders (Fig.10). Based on this, the phases obtained on films are comparable to the ones shown on powders, at the same calcination treatment at high temperatures. This suggests that the disproportionation mechanism<sup>32</sup> can take place also on films. The occurrence of MnO<sub>2</sub> at 800°C annealing is in contrast to the anneal at 450°C, where this phase was not observed (Fig.6). This can be explained by the crystallization of Mn<sup>4+</sup> in various secondary phases, caused by the anneal at high temperature in O<sub>2</sub>. As a complementary technique to confirm the presence of different Mn<sup>n+</sup>-O vibrations, related to different phases, Raman spectroscopy was performed, as shown in Fig.14

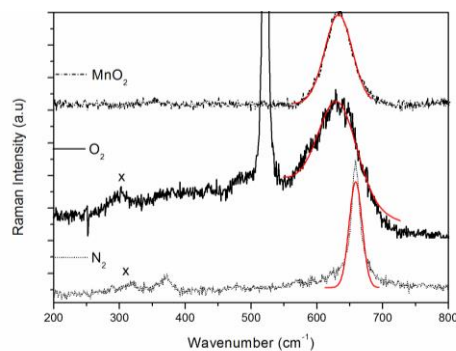


Figure 14: Raman spectrum of films on Si substrates, annealed 800°C for 3h in N<sub>2</sub> and O<sub>2</sub> compared to MnO<sub>2</sub> powder.

Table 7: Deconvolution and peak assignment<sup>58,59</sup> of films on Si substrates, annealed at 800°C for 3h in N<sub>2</sub> and O<sub>2</sub>

Legend	Wavenumber (cm <sup>-1</sup> ) in N <sub>2</sub> ambient	Wavenumber (cm <sup>-1</sup> ) in O <sub>2</sub> ambient	Wavenumber (cm <sup>-1</sup> ) in MnO <sub>2</sub>	Species Involved	Vibrational Mo Cation
Red	650	620	620	A <sub>1g</sub>	Mn-O in MnC Li-O connect

The Raman band located at 625-650 cm<sup>-1</sup> becomes less sharp and intense in the films heated in O<sub>2</sub> compared to the N<sub>2</sub> case, due to phase segregation phenomena (λ-MnO<sub>2</sub> and γ-Mn<sub>2</sub>O<sub>3</sub>). As already observed before, the A<sub>1g</sub> mode shifts to lower

wavenumber (from  $650\text{ cm}^{-1}$  in  $\text{N}_2$  to  $620\text{ cm}^{-1}$  in  $\text{O}_2$ ). This band is attributed to the stretching mode of  $\text{MnO}_6$  octahedra in  $\lambda\text{-MnO}_2$ , as it is the only phase detected for commercial  $\text{MnO}_2$  powder. Therefore, films annealed in  $\text{O}_2$  consist of a mixture of  $\gamma\text{-Mn}_2\text{O}_3$ ,  $\text{MnO}_2$  and the desired LMO phase,<sup>70</sup>. In contrast, the  $\text{N}_2$  anneal does not show the presence of  $\lambda\text{-MnO}_2$  being formed (also in Fig.12-13).

Since the material final application will be in an all solid state battery, the morphology and the substrate coverage is also an important parameter to be investigated. Therefore SEM analysis was performed on films annealed at  $800^\circ\text{C}$  for 3h (Fig.15).

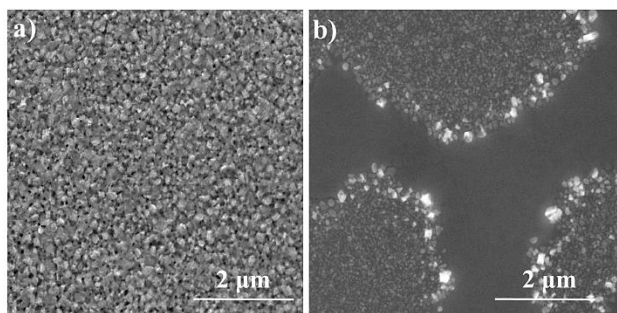


Figure 15: SEM Pictures of films on Si substrates, annealed in a)  $\text{N}_2$  and b)  $\text{O}_2$  at  $800^\circ\text{C}$  for 3h at  $10^\circ\text{C}/\text{min}$ .

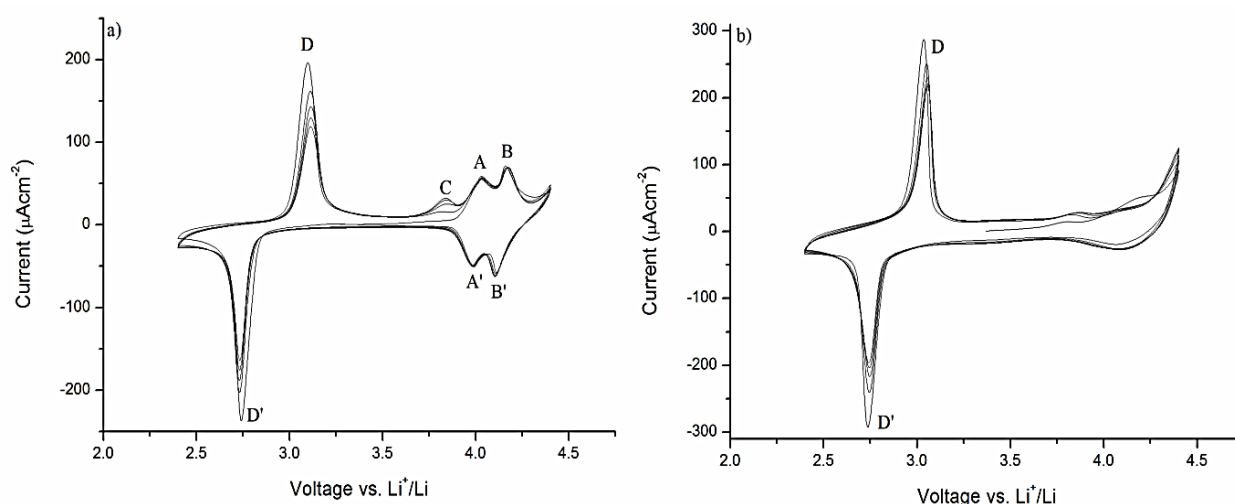


Figure 16: Cyclic voltammogram (first 5 cycles,  $10\text{ mV}/\text{sec}$ ) of the films onto  $\text{Si}/\text{SiO}_2/\text{TiN}/\text{Pt}$ , after annealing at  $450^\circ\text{C}$  for 1h in a)  $\text{N}_2$  and b)  $\text{O}_2$ .

Films annealed in  $\text{N}_2$  maintain uniformity and full coverage of the substrate, while films annealed in  $\text{O}_2$  show an inhomogeneous morphology with large sections, where the substrate is uncoated, possibly due to shrinkage during the crystallization process. Samples annealed in oxygen show a different grain size and morphology. Together with the XRD and Raman (Fig. 12, 13 and 14), this shows that phase segregation is occurring.

#### Electrochemical activity of the prepared films on Pt

The phase segregation observed previously may influence the electrochemical properties of the film, and therefore cyclic voltammograms are measured (Fig.16).

The LMO film annealed in  $\text{N}_2$  was the only sample exhibiting activity in the 4 V region. The CV shows two pairs of clear and strong peaks located at 4.03 (A), 3.96 (A'), 4.15 (B) and 4.10 (B') V vs  $\text{Li}^+/\text{Li}$ . These peaks correspond to the two-step reversible (de)intercalation of lithium between  $\text{LiMn}_2\text{O}_4$  and  $\lambda\text{-MnO}_2$ <sup>18,80,81</sup>.

In the 4V region, no significant difference is seen as the number of cycles increases (up to 10, shown only last 5), indicating good repeatability. The good cycling stability was already attributed to the fact that Li ions are de-inserted from the cubic structure with a minimal contraction of the unit cell<sup>82</sup>.

Outside the 4V region, a pair of strong peaks located at 3.11V vs  $\text{Li}^+/\text{Li}$  (D) and 2.74V vs  $\text{Li}^+/\text{Li}$  (D') appears. This pair (D and D') represents the 3V process corresponding to (i) further  $\text{Li}^+$  intercalation and formation of  $\text{Li}_2\text{Mn}_2\text{O}_4$  together with the reduction of the average oxidation state of manganese from 3.5 to 3V vs  $\text{Li}^+/\text{Li}$  (D') and (ii) the  $\text{Li}^+$  extraction from the formed  $\text{Li}_2\text{Mn}_2\text{O}_4$  and the re-oxidation of average oxidation state up to 3.5V (D).<sup>16,18</sup> At the start of the second cycle (i.e. at 3.2V vs  $\text{Li}^+/\text{Li}$ ), a new peak appears around 3.78V vs  $\text{Li}^+/\text{Li}$  (C) which is ascribed to the lithium extraction from octahedral

For the films annealed in  $\text{O}_2$  no characteristic peak for  $\text{Li}^+$

intercalation and (de)intercalation was observed in the 4V vs  $\text{Li}^+/\text{Li}$  region.

This can be due to the presence of amorphous  $\lambda\text{-MnO}_2$  (as suggested also from previous analyses) which, together with the other secondary phase  $\gamma\text{-Mn}_2\text{O}_3$ , is compromising the  $\text{Li}^+$  diffusion and therefore the activity of the material. In fact, both  $\lambda\text{-MnO}_2$  and  $\gamma\text{-Mn}_2\text{O}_3$  are spinel structures but their activity lies in a different voltage range (1-1.5 range) useful for anode materials<sup>83,84</sup>. When present in combination with LMO,  $\text{Li}^+$  can diffuse into one of their network and not to the LMO,

compromising the electrochemical activity. This effect can be seen in Fig.S10-11, where the activity of mixed phases is shown. In both cases, N<sub>2</sub> and O<sub>2</sub> annealing, at high temperatures a new peak/shoulder around 3.2V can be seen, and from the first cycle this secondary phase (assigned possibly to MnO<sub>2</sub>) the intercalation of Li<sup>+</sup> in spinel LMO in the 4V region is compromised. This corroborates the already discussed advantages of the low temperature treatment. The ability of a cathode material to intercalate Li-ions is closely related to their electrical and ionic conduction. In a battery, when Li-ion diffuses out of the cathode (ionic conduction) during cycling, the valence state of the transition metal ion (Mn) changes (electronic conduction). Previous studies showed that annealing temperatures and atmospheres (oxygen pressures) had no considerable effects on electrical properties of the LMO material<sup>85,86</sup>. A possible reason for the different electrochemical activity of the samples annealed in N<sub>2</sub> and O<sub>2</sub> can be found in the crystal structure of the oxide<sup>87</sup>, affecting the Li ion diffusion. Samples annealed in N<sub>2</sub> show cubic spinel phase pure LMO, and therefore 3D arrays of tunnels for Li ion conduction, which are lost in samples annealed in O<sub>2</sub> due to phase segregation and the presence of tetragonal Mn<sub>2</sub>O<sub>3</sub> together with amorphous cubic MnO<sub>2</sub>. A second important parameter that affects Li<sup>+</sup> diffusion is the grain size, both in powders and films<sup>87,88</sup>. A smaller particle size leads to a significant increase in ionic conductivity and therefore in electrical conduction. SEM pictures (Fig.15) nano-sized grains are clearly visible in samples annealed in N<sub>2</sub>, while for samples annealed in O<sub>2</sub> it was not possible to define grain size due to the possible partially amorphous nature of the deposited materials. More parameters can affect Li diffusion into the lattice, such as defects, Li-O binding energy and bond types, phase transition, but considering the similar nature of those oxides, characterized by ionic bond types with coulombic interactions occurring, and the same Jahn-Teller phase transition for all Mn oxides, these parameters were not explored further.

## Conclusions

Phase pure spinel LiMn<sub>2</sub>O<sub>4</sub> powders and around 100 nm thick films are successfully prepared via chemical solution deposition using an entirely water based precursor solution. The crystalline, spinel phase is achieved already before 450 °C in an N<sub>2</sub> atmosphere, creating opportunities for a relatively low temperature synthesis and the use of oxidation sensitive substrates and current collectors, such as TiN. If O<sub>2</sub> is added during the post-anneal, the purity of the spinel phase is compromised by the presence of secondary phases, such as Mn<sub>2</sub>O<sub>3</sub> and λ-MnO<sub>2</sub>. Here, we find that this material sensitivity and instability is also found while depositing LMO films. The Mn<sup>3.5+</sup> (average oxidation state) ions present in the gel or the wet film are extremely sensitive to O<sub>2</sub> and are easily subjected to fast oxidation, which is in agreement with Nakamura's results<sup>31</sup>. The oxygen pressure of the final anneal was therefore crucial to have stoichiometric LiMn<sub>2</sub>O<sub>4</sub> without any

phase segregation. In particular, at 450°C λ-MnO<sub>2</sub> appears to be still amorphous and not detected via XRD, but nevertheless strongly affects the morphology and electrochemical performances of the prepared film, leading to very slow Li<sup>+</sup> ions diffusion and therefore inactivity of the material. When the annealing temperature is increased, crystalline λ-MnO<sub>2</sub> starts to appear at 800°C, as confirmed by in-situ XRD. The formation of the λ-MnO<sub>2</sub> crystalline layer at higher temperature in O<sub>2</sub> was also confirmed with XRD and Raman spectroscopy, both for powders and for films. The disproportionation mechanism already confirmed by Strobel et al.<sup>32</sup>, justified the phase segregation also in our LMO films and motivates the successful use of N<sub>2</sub> atmosphere for the final anneal of our films. The secondary phases also strongly affect the morphology of film, altering coverage and uniformity of the surface. In conclusion, the atmosphere choice is crucial in order to obtain LMO films with high quality and to prevent undesired secondary reactions, which can lead to weaker electrochemical properties or total inactivity of the cathode material.

## Acknowledgments

The authors acknowledge financial support by the IWT Flanders (SBO project SOSLion). Special thanks to K. Elen and B. Ruttens for XRD analysis, Thomas Vranken for TEM, Wouter Marchal for thermal analysis, Christopher De Dobbelaere and Dries De Sloovere for FT-IR and GATR and Elsy Thijsen for ICP-AES.

## Bibliography

- 1 V. Etacheri, *Energy Environ. Sci.*, 2011, **4**, 3243.
- 2 J. B. Bates, N. J. Dudney, D. C. Lubben, G. R. Gruzalski, B. S. Kwak, X. Yu and R. a. Zuh, *J. Power Sources*, 1995, **54**, 58–62.
- 3 S. Jones, J. Akridge and F. Shokoohi, *Solid State Ionics*, 1994, **69**, 357–368.
- 4 J. Bates, N. Dudney, B. Neudecker, A. Ueda and C. Evans, *Solid State Ionics*, 2000, **135**, 33–45.
- 5 J. F. M. Oudenhoven, L. Baggetto and P. H. L. Notten, *Adv. Energy Mater.*, 2011, **1**, 10–33.
- 6 A. Patil, V. Patil, D. Wook Shin, J. W. Choi, D. S. Paik and S. J. Yoon, *Mater. Res. Bull.*, 2008, **43**, 1913–1942.
- 7 X. Zhang, H. Zheng, V. Battaglia and R. L. Axelbaum, *J. Power Sources*, 2011, **196**, 3640–3645.
- 8 J. Cho and G. Kim, *Electrochem. solid-state Lett.*, 1999, **2**, 253.
- 9 D. Arumugam and G. P. Kallagan, *Thin Solid Films*, 2011, **520**, 338–343.
- 10 S. B. Chikkannanavar, D. M. Bernardi and L. Liu, *J. Power Sources*, 2014, **248**, 91–100.
- 11 G. Xu, Z. Liu, C. Zhang, G. Cui and L. Chen, *J. Mater. Chem. A*, 2015, **3**, 4092–4123.
- 12 T. Matsumura, N. Imanishi, A. Hirano, N. Sonoyama and Y. Takeda, *Solid State Ionics*, 2008, **179**, 2011–2015.

- 13 S. N. Karthick, S. Richard Prabhu Gnanakan, a. Subramania and H. J. Kim, *J. Alloys Compd.*, 2010, **489**, 674–677.
- 14 S. Y. Chew, T. J. Patey, O. Waser, S. H. Ng, R. Büchel, a. Tricoli, F. Krumeich, J. Wang, H. K. Liu, S. E. Pratsinis and P. Novák, *J. Power Sources*, 2009, **189**, 449–453.
- 15 H. S. Moon and J. W. Park, *J. Power Sources*, 2003, **119–121**, 717–720.
- 16 S. B. Tang, M. O. Lai and L. Lu, *Electrochim. Acta*, 2006, **52**, 1161–1168.
- 17 S. Koike and K. Tatsumi, *J. Power Sources*, 2005, **146**, 241–244.
- 18 E. . C. A. Rougier, K.A. Striebel, S.J. Wen, *J. Electrochem. Soc.*, 1998, **145**, 2975.
- 19 K.-H. Hwang, S.-H. Lee and S.-K. Joo, *J. Power Sources*, 1995, **54**, 224–227.
- 20 R. W. Schwartz, in *Solution Processing of Inorganic Materials*, ed. D. Mitzi, Wiley, Hoboken, New Jersey, 2009, p. 471.
- 21 R. W. . Schwartz, *Chemie*, 2004, **7**, 433–461.
- 22 R. W. Schwartz, T. Schneller and R. Waser, *Comptes Rendus Chim.*, 2004, **7**, 433–461.
- 23 † and Keiichi Kohama§ Yumi H. Ikuhara\*,† Xiang Gao,† Rong Huang,†,‡ Craig A. J. Fisher,† Akihide Kuwabara,† Hiroki Moriwake, *J. Phys. Chem. C*, 2014, **118**, 19540–19574.
- 24 Y. H. Ikuhara and Y. Iwamoto, *J. Mater. R*, 2000, **15**, 2–4.
- 25 X. Gao, Y. H. Ikuhara, C. A. J. Fisher, H. Moriwake, A. Kuwabara, H. Oki, K. Kohama, R. Yoshida, R. Huang and Y. Ikuhara, *Adv. Mater. Interfaces*, 2014, **1**, 1400143.
- 26 M. S. Bhuiyan, M. Paranthaman and K. Salama, *Supercond. Sci. Technol.*, 2006, **19**, R1–R21.
- 27 Jolivet J.P., in *Functional Coatings: By Polymer Microencapsulation*, ed. S. K. Ghosh, Wiley, Chichester, 2006.
- 28 Y. J. Park, J. G. Kim, M. K. Kim, H. T. Chung and H. G. Kim, *Solid State Ionics*, 2000, **130**, 203–214.
- 29 Y. . Park, J. . Kim, M. . Kim, H. . Chung, W. . Um, M. . Kim and H. . Kim, *J. Power Sources*, 1998, **76**, 41–47.
- 30 Y. H. Ikuhara, Y. Iwamoto, K. Kikuta, S. Hirano and I. Introduction, *J. Mater. Res.*, 1999, **14**.
- 31 T. Nakamura and A. Kajiyama, *Solid State Ionics*, 2000, **133**, 195–202.
- 32 P. Strobel, G. Rouse, a Ibarra-Palos and C. Masquelier, *J. Solid State Chem.*, 2004, **177**, 1–5.
- 33 C. Lu and S. K. Saha, 2001, 27–34.
- 34 K.-F. Chiu, H. C. Lin, K. M. Lin and C. C. Chen, *J. Electrochem. Soc.*, 2006, **153**, A1992.
- 35 Y. Xia and H. Noguchi, *J. Solid State Chem.*, 1995, **119**, 216–218.
- 36 Y. Gao and J. R. Dahn, *Solid State Ionics*, 1996, **84**, 33–40.
- 37 Gao Yuan and J. R. Dahn, *J. Electrochem. Soc.*, 1996, **143**, 100–114.
- 38 M.M Thackeray and M.h Rossouw, *J. Solid State Chem.*, 1994, **113**, 441–443.
- 39 C. Masquelier, M. Tabuchi, K. Ado, R. Kanno, Y. Kobayashi, Y. Maki, O. Nakamura and J. B. Goodenough, *J. Solid State Chem.*, 1996, **123**, 255–266.
- 40 P. McIntyre and S. Summerfelt, *J. Appl. Phys.*, 1997, **82**, 4577–4585.
- 41 W. Knaepen, C. Detavernier, R. L. Van Meirhaeghe, J. Jordan Sweet and C. Lavoie, *Thin Solid Films*, 2008, **516**, 4946–4952.
- 42 G. Rempelberg, B. De Schutter, W. Devulder, K. Martens, I. Radu and C. Detavernier, *J. Mater. Chem. C*, 2015, **3**, 11357–11365.
- 43 K. Van Werde, D. Mondelaers, G. Vanhoyland, D. Nelis, M. K. Van Bael, J. Mullens, L. C. Van Poucke, B. Van Der Veken and H. O. Desseyn, *J. Mater. Sci.*, 2002, **37**, 81–88.
- 44 D. R. van Heidi, M.K. Van Bael, A. Hardy, W. van Kristof and J. Mullens, *Handb. Nanoceramics Their Based Nanodevices*, 2009, **1**, 267–300.
- 45 a. Hardy, K. Van Werde, G. Vanhoyland, M. K. Van Bael, J. Mullens and L. C. Van Poucke, *Thermochim. Acta*, 2003, **397**, 143–153.
- 46 Y. Xia and M. Yoshio, *J. Electrochem. Soc.*, 1997, **144**, 4186.
- 47 R. Gummow, a Dekock and M. Thackeray, *Solid State Ionics*, 1994, **69**, 59–67.
- 48 W. Liu, G. Farrington, F. Chaput and B. Dunn, ... *Electrochem. ....*, 1996, **143**, 879–884.
- 49 S. Chen, F. Cao, F. Liu, Q. Xiang, X. Feng, L. Liu and G. Qiu, *RSC Adv.*, 2014, **4**, 13693.
- 50 Y. Hon, S. Lin, K. Fung and M. Hon, *J. Eur. Ceram. Soc.*, 2002, **22**, 653–660.
- 51 S. Chitra, P. Kalyani and T. Mohan, *J. ....*, 1999, 433–441.
- 52 C. Wu, Z. Wang, F. Wu, L. Chen and X. Huang, 2001, 277–285.
- 53 Y. Cui, Z. Yuan, W. Bao, Q. Zhuang and Z. Sun, *J. Appl. Electrochem.*, 2012, **42**, 883–891.
- 54 J. Marcicki, A. Bartlett, M. Canova, a. T. Conlisk, G. Rizzoni, Y. Guezennec, X. G. Yang and T. Miller, *ECS Trans.*, 2013, **50**, 235–247.
- 55 O. Haik, N. Leifer, Z. Samuk-Fromovich, E. Zinigrad, B. Markovskiy, L. Larush, Y. Goffer, G. Goobes and D. Aurbach, *J. Electrochem. Soc.*, 2010, **157**, A1099.
- 56 F. Cao and J. Prakash, *Electrochim. Acta*, 2002, **47**, 1607–1613.
- 57 K. Dokko, M. Mohamedi, Y. Fujita, T. Itoh, M. Nishizawa, M. Umeda and I. Uchida, *J. Electrochem. Soc.*, 2001, **148**, A422.
- 58 B. Ammundsen, G. R. Burns, M. S. Islam, H. Kanoh and J. Rozie, 1999, 5175–5180.
- 59 M. M. Sinha and H. C. Gupta, *Phys. B Condens. Matter*, 2002, **316–317**, 166–169.
- 60 C. M. Julien, A. Mauger, K. Zaghib and H. Groult, *Inorganics*, 2014, **2**, 132–154.
- 61 C. Julien, M. Massot, S. Rangan, M. Lemal and D. Guyomard, *J. Raman Spectrosc.*, 2002, **33**, 223–228.
- 62 C. Julien, M. Massot and U. Pierre, in *New Trends in Intercalation Compounds for Energy Storage*, 2002, vol. 4, pp. 235–252.
- 63 D. Guan, C. Cai and Y. Wang, *2011 IEEE Green Technol. Conf. Green 2011*, 2011, 1465–1469.
- 64 D. Kim, S. Park, O. B. Chae, J. H. Ryu, Y.-U. Kim, R.-Z. Yin and S. M. Oh, *J. Electrochem. Soc.*, 2012, **159**, A193.

- 65 Q. Jiang, X. Wang, C. Miao and Z. Tang, *RSC Adv.*, 2013, **3**, 12088.
- 66 S. H. Shim, D. LaBounty and T. S. Duffy, *Phys. Chem. Miner.*, 2011, **38**, 685–691.
- 67 P. Lanz, C. Villevieille and P. Novák, *Electrochim. Acta*, 2013, **109**, 426–432.
- 68 N. Mironova-Ulmane, A. Kuzmin and M. Grube, *J. Alloys Compd.*, 2009, **480**, 97–99.
- 69 C. M. Julien and M. Massot, *Mater. Sci. Eng. B*, 2003, **97**, 217–230.
- 70 C. M. Julien and M. Massot, *J. Phys. Condens. Matter*, 2003, **15**, 3151–3162.
- 71 R. Pretorius, J. M. Harris and M.-A. Nicolet, *Solid. State. Electron.*, 1978, **21**, 667–675.
- 72 L. Baggetto, J. F. M. Oudenhoven, T. van Dongen, J. H. Klootwijk, M. Mulder, R. a H. Niessen, M. H. J. M. de Croon and P. H. L. Notten, *J. Power Sources*, 2009, **189**, 402–410.
- 73 G. A. and J.-M. A. Du Pasquier, F. Disma, T. Bowmer, A. S. Gozdz and T. J., *J. Electrochem. Soc.*, 1998, **145**, 472–477.
- 74 K. Y. Chung, H. S. Lee, W.-S. Yoon, J. McBreen and X.-Q. Yang, *J. Electrochem. Soc.*, 2006, **153**, A774.
- 75 Y. Xia, T. Sakai, T. Fujieda, X. Q. Yang, X. Sun, Z. F. Ma, J. McBreen and M. Yoshio, *J. Electrochem. Soc.*, 2001, **148**, A723.
- 76 a. Hardy, D. Nelis, G. Vanhoyland, M. K. Van Bael, H. Van den Rul, J. Mullens, L. C. Van Poucke, J. D'Haen, L. Goux and D. J. Wouters, *Mater. Chem. Phys.*, 2005, **92**, 431–437.
- 77 S. Chitra, P. Kalyani, T. Mohan, M. Massot, S. Ziolkiewicz, R. Gangandharan, M. Eddrief and C. Julien, *Ionics (Kiel)*, 1998, **4**, 8–15.
- 78 T. Yi, C. Dai, K. Gao and X. Hu, *J. Alloys Compd.*, 2006, **425**, 343–347.
- 79 G. Li, L. Jiang, H. Pang and H. Peng, *Mater. Lett.*, 2007, **61**, 3319–3322.
- 80 K. a. Striebel, *J. Electrochem. Soc.*, 1996, **143**, 1821.
- 81 and C. C. C. F. K. Shokoohi,\* J. M. Tarascon,\* B. J. Wilkens, D. Guyomard, *J. Electrochem. Soc.*, 1992, **139**, 1845–1849.
- 82 M. Winter, J. O. Besenhard, M. E. Spahr and P. Novák, *Adv. Mater.*, 1998, **10**, 725–763.
- 83 and G. Z. Yuhang Wang, Yehua Wang, Dingsi Jia, Zheng Peng, Yongyao Xia, *Nano Lett.*, 2014, **14**, 1080–1084.
- 84 Y. Qiu, G.-L. Xu, K. Yan, H. Sun, J. Xiao, S. Yang, S.-G. Sun, L. Jin and H. Deng, *J. Mater. Chem.*, 2011, **21**, 6346.
- 85 J. Marzec, K. Swierczek, J. Przewoznik, J. Molenda, D. R. Simon, E. M. Kelder and J. Schoonman, *Solid State Ionics*, 2002, **146**, 225–237.
- 86 J. Molenda, K. Swierczek, W. Kucza, J. Marzec and A. Stoklosa, *Solid State Ionics*, 1999, **123**, 155–163.
- 87 M. Park, X. Zhang, M. Chung, G. B. Less and A. M. Sastry, *J. Power Sources*, 2010, **195**, 7904–7929.
- 88 C. Ying-Chao, *Chin. Phys. B*, 2011, **20**.